Hyperfine Interact
DOI 10.1007/s10751-012-0652-1

Industrial applications of Mössbauer Spectroscopy

Massimo Carbucicchio · Roberta Ciprian

Abstract A review of the industrial applications of Mössbauer Spectroscopy is presented underlining the powerfulness and usefulness of the technique in the control and optimization of the production processes. A few examples are reported concerning the developments of thin protective coatings for structural parts and media for the magnetic recording field.

Keywords Mössbauer Spectroscopy · Interdiffusion phenomena · Magnetic properties · Industrial applications

1 Introduction

The increasing demand of new materials and the continuous need to reduce the media dimensions while improving the device/material quality and performances determined the desire of large and middle industries to introduce new analysis techniques for the check and control of their production processes. However many commonly used techniques are characterized by a very low local sensitivity and give only one information at a time.

The Mössbauer Spectroscopy is a promising candidate as a new industrial measuring technique, being the most sensitive spectroscopy up to now known. It is characterized by a very large local sensitivity, and can be performed during every step of the production process giving information on phase composition, grain size distributions, and magnetic properties. Depth-profiling information can be obtained selecting the reemitted resonant radiation or the electron energy, without necessity of sample preparation and in a non-destructive way.

Thanks to these characteristics, the Mössbauer spectroscopy has been applied in many research and production fields, metallurgy, energy production, catalysis,

M. Carbucicchio (✉) · R. Ciprian
Department of Physics, University of Parma, Parco Area delle Scienze 7/A, 43100 Parma, Italy
e-mail: massimo.carbucicchio@fis.unipr.it

Published online: 17 October 2012

tribology, ultra-thin magnetic/superconductor/ferroelectric film production, biomedicine as well as cultural heritage and mineralogy.

2 Main industrial applications

In the field of heterogeneous catalysis, where the attractive trend is the development of new rare-earth based catalysts [1] and nanotubes/wires containing nanoparticles [2], Mössbauer spectroscopy proved to be a very powerful tool for intermediate-phase identification, detection of superparamagnetic and amorphous compounds, evaluation of the extent of oxidation during the catalytic reaction.

The possibility to follow a chemical reaction or a phase transformation is relevant for the study of the corrosion mechanisms of structural materials. The final aim is to find the best way to protect these materials increasing their in-service life, using both innovative and complex thin coatings [3] and surface engineering treatments [4] such as high energy beam laser welding, cutting and drilling. Scattering Mössbauer spectroscopy is a non-destructive tool which does not require sample preparation allowing high-sized material to be analyzed.

Another industrial field where Mössbauer spectroscopy proved to be fundamental concerns the superconductivity and the new high-T_c superconductors containing low amounts of Fe [5]. Mössbauer spectroscopy was fundamental for evidencing the existence of structural-magnetic transitions, and for clarifying the spin dynamics and the effects of oxygen vacancies in the establishing of superconductivity. The possibility to study defects and vacancies distribution is also important for the recent discovery of dilute magnetic semiconductors and multiferroics [6] which can be fruitfully employed in new generation of CMOS, MRAM and spintronic devices. The use of high field Mössbauer spectroscopy is fundamental for unambiguously identify (i) the cation distribution, (ii) the magnetic moment directions of the different sites, and (iii) the magnetic ordering.

In the following sections, a few examples will be presented and discussed with the aim to evidence the suitability and peculiarity of Mössbauer spectroscopy applied in different industrial fields.

3 Protective coatings and thin films

Iron–nickel alloys show good resistance to chemical and environmental corrosion, however, they show a relatively low surface hardness and wear resistance. Surface engineering procedures are required in order to improve their in-service life [7]. Boron cementation is an alternative to carburizing or nitriding, considering the limited diffusivity of carbon or nitrogen into nickel.

A commercial $Fe_{64}Ni_{36}$ invar alloy was borided at 850 °C with a pack cementation process using a high-potential-boronizing powder mixture constituted by amorphous B and KBF_4 activator (10 wt.%), for times of 20 min, 1 and 8 h.

For the 20 min borided $Fe_{64}Ni_{36}$, the CXMS (Fig. 1a) can be interpreted as the superposition of (i) a small contribution (Ψ) due to the base alloy [8], (ii) two sextets (β_3, β_4) and (iii) a quadrupolar doublet (δ). Considering: (i) previously obtained results on Fe containing low amounts of Ni [9], (ii) the hyperfine parameters of

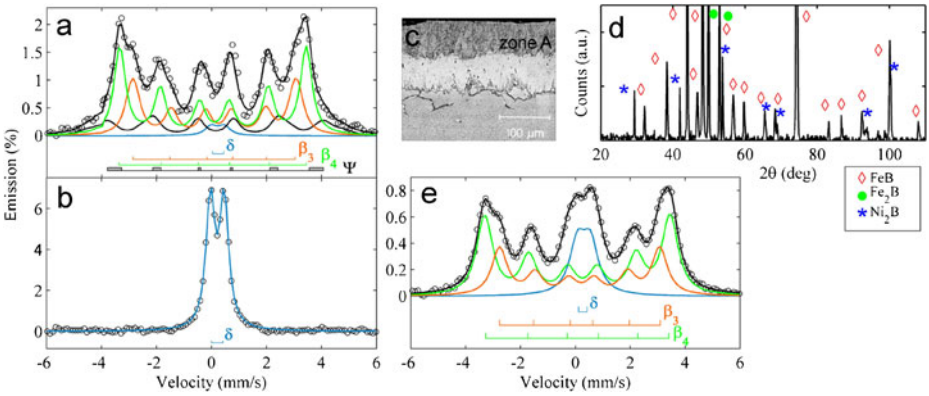

Fig. 1 CXMS for $Fe_{64}Ni_{36}$ borided for **a** 20 min and **b** 1 h. **c** metallographic cross-section and **d** XRD for the 8h-borided $Fe_{64}Ni_{36}$, **e** CXMS for the same sample after 450 μm surface abrasion

the contributions, and (iii) the Fe/Ni atomic ratio which is the same of the base alloy into the whole coating (as obtained from cross-section EDX analysis), the β_3 and β_4 sextets are attributed to a $(Fe,Ni)_2B$ and the δ doublet to a (Fe,Ni)B compound. Therefore, boron reacts indifferently with Fe and Ni, giving rise to ternary compounds, with the Fe/Ni atomic ratio equal to that of the base alloy. Because of (i) the close similarity of Fe and Ni atoms, and (ii) the isomorphism of Fe_2B and Ni_2B, XRD is not able to distinguish the presence of Ni in iron borides.

The CXMS spectra measured for the $Fe_{64}Ni_{36}$ alloy borided for 1 and 8 h only show the contribution of the δ quadrupolar doublet due to (Fe,Ni)B (Fig. 1b). On the other hand the XRD pattern for the $Fe_{64}Ni_{36}$ alloy borided for 8 h (Fig. 1d) shows the FeB and Fe_2B phases and the formation of nickel borides which are located in the more external part of the coating, as demonstrated by layer-by-layer abrasion. In effect after removing practically the whole outer sublayer of the coating, (Fig. 1c), the CXMS spectrum (Fig. 1e) shows the prevailing contribution due to the $(Fe,Ni)_2B$ ternary compound, and a small amount of (Fe,Ni)B.

In the case of protective thin films for cutting and functional tools where the industrial requirements are a very large friction and wear resistance, another important parameter is the adhesion of the coating to the base material. The film thickness is finely controlled in order to obtain (i) a maximum of hardness while retaining the toughness of the working surface, and (ii) the good adhesion to the base material. Typical examples are very hard films of TiN which are used for improving the mechanical behaviour of tools in metal cutting and forming [3].

Bar of AISI M35 tool steels were coated with 3–4 μm thick films of TiN or Ti(C,N) deposited by two industrial facilities: arc (AE) and electron beam (EB) evaporation, onto a thin intermediate layer of metallic Ti. This layer allows the formation of an interface region constituted by Fe-Ti solid solutions which are fundamental for the adhesion [10]. The experimental details are reported in [3].

In the following the samples will be labelled with AE or EB followed by the developed coating. For DCEMS analysis, coatings ~40 nm thick were grown under the same conditions onto ^{57}Fe foils. In the following these samples will be labelled introducing in the notation ^{57}Fe.

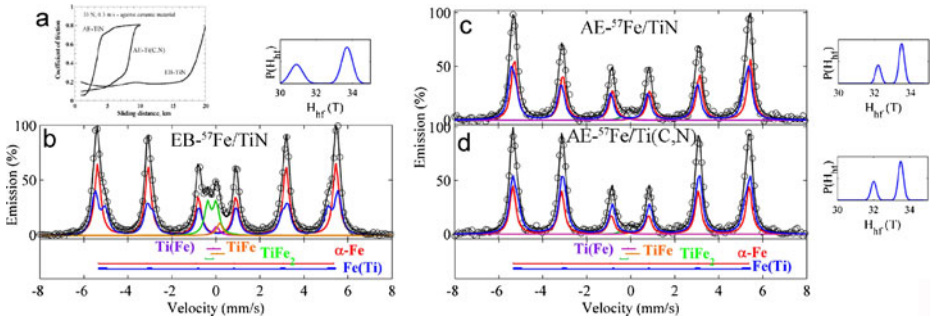

Fig. 2 **a** friction curves measured for EB-, AE-TiN, AE-Ti(C,N); **b**, **c**, **d** CEMS spectra for EB-^{57}Fe/TiN, AE-^{57}Fe/TiN, AE-^{57}Fe/Ti(C, N) respectively

All friction curves (Fig. 2a) show an abrupt increase in the friction coefficient from ∼0.10 to ∼0.82, occurring at different sliding distances, representing the wear resistance of the coatings. For EB-TiN, the transition occurs at ∼20 km, value much higher than that of AE-Ti(C,N) (∼7.5 km) and AE-TiN (∼2.5 km). These differences cannot be explained considering (i) film thickness, (ii) microstructure and (iii) microhardness (almost the same for all coatings ∼20 kN/mm^2).

Figure 2b–d shows the 7.0 – 7.3 keV CEMS spectra performed for the corresponding ^{57}Fe-samples. All spectra can be interpreted as the superposition to the base α-Fe of an interfacial region constituted by: (i) a series of sextets due to a solid solution of Ti in α-Fe, (ii) a paramagnetic contribution ascribed to a solid solution of Fe in α-Ti, and (iii) Fe-Ti intermetallic compounds (TiFe and $TiFe_2$).

The EB-^{57}Fe/TiN (Fig. 2b) shows an interface region significantly higher than that of both AE-^{57}Fe/TiN (Fig. 2c) and AE-^{57}Fe/Ti(C,N) (Fig. 2d), while for these AE samples, the interface is almost comparable. Correspondingly, the scratch tests (loads: 25-100N, Rockwell C diamond stylus) give ∼80N as the critical load for EB-^{57}Fe/TiN, and ∼40N for the AE samples. This confirms that adhesion is favoured by the Fe-Ti interface, increasing with its abundance.

The angle between the magnetization direction and the film plane for EB-^{57}Fe/TiN and AE-^{57}Fe/Ti(C,N) is ∼24°, while that for AE-^{57}Fe/TiN is ∼36° as evaluated from the line intensity ratio (Fig. 2b–d). This increase in the magnetization component normal to the sample plane suggests the establishing of a more intense compressive stress state at the interface, which is responsible for the lower wear resistance of AE-TiN in respect to AE-Ti(C,N).

4 Nanocomposites and multilayers

The interface phenomena largely influence the properties of nanocomposites and multilayers where surfaces and interfaces are predominant with respect to the whole sample volume. Mössbauer spectroscopy has been used to deeply understand the coercivity behaviour in exchange-spring magnets having perpendicular anisotropy [11, 12]. These systems are constituted by hard and soft magnetic phases that can interact at their interface giving rise to single phase magnetic media, with large coercivity and high magnetization saturation.

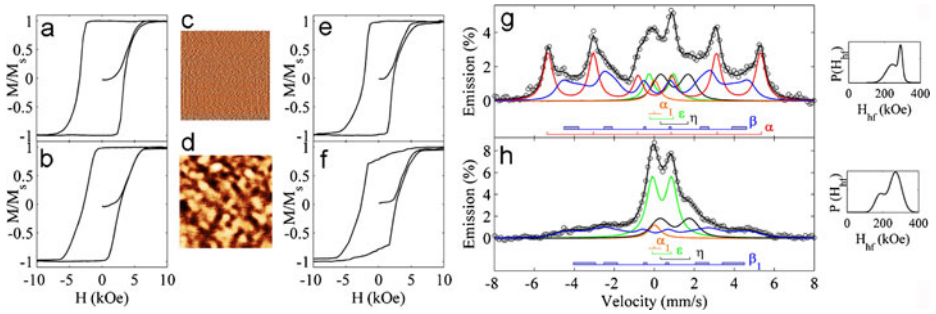

Fig. 3 Polar loops and 1 μm^2 AFM for **a–c** FePt(15) and **b–d** FePt(20) respectively. Polar loops and CEMS spectra respectively for **e–g** FePt(15)/Fe(7) and **f–h** FePt(20)/Fe(7)

The studied systems are constituted by 20 and 15 nm thick hard $Fe_{52}Pt_{48}$ phase grown by rf sputtering onto MgO-(100) monocrystals at 550 °C [FePt(t_{FePt}), with $t_{FePt} = 15$, 20 nm], and a 7 and 14 nm thick ^{57}Fe layer grown by molecular beam epitaxy (MBE) at RT [FePt(t_{FePt})/Fe(t_{Fe}), with t_{Fe} the Fe thickness in nm].

The FePt single-layers are characterized by very hard magnetic properties (Fig. 3a–b). The increase in thickness determines a decrease of coercivity (from 4.2 to 2.3 kOe) and an appreciable shearing of the hysteresis loop (Fig. 3b).

The films covered by a 7 nm thick ^{57}Fe layer (Fig. 3e–f) are characterized by a single phase hard magnetic behaviour, however the trend of coercivity as a function of the Fe layer thickness is quite different. In effect, while for the FePt(15)/Fe(t_{Fe}) the coercivity monotonically decreases by increasing the Fe layer thickness, in the case of FePt(20)/Fe(t_{Fe}) the coercivity increases up to a Fe thickness of 7 nm and then abruptly decreases. This different coercivity behaviour is due to the morphology of the hard FePt. The FePt(15) is characterized by a very smooth surface (Fig. 3c) while the FePt(20) shows a granular structure characterized by a significant roughness (Fig. 3d).

The CEMS spectra (Fig. 3g–h) performed for the FePt(t_{FePt})/Fe(t_{Fe}) series indicate that during the Fe deposition a large intermixing occurs. For the FePt(15)/Fe(7), an interface region forms between FePt and Fe, constituted by an Fe-rich FePt compound showing a distribution of particles dimensions (β-contribution) whose sizes decrease down to the superparamagnetic limit (δ-contribution) (Fig. 3g). On the contrary for FePt(20)/Fe(7) (Fig. 3h), Fe completely diffuses into the hard film (no α-Fe contribution). The Fe-rich FePt compound having a broad distribution of particle sizes forms in the uppermost part of the bilayer and is separated from the hard layer by an interfacial region constituted by Fe-rich FePt superparamagnetic small particles. The formation of this peculiar structure is at the origin of the initial increase of coercivity as a function of the Fe thickness, probably because of an increase of grain boundaries which act as domain wall pinning sites. On the other hand, the increased amount of grain boundaries in the case of FePt(15)/Fe(t_{Fe}) is not able to hinder the decrease in coercivity due to the presence of a pure Fe layer.

Mössbauer spectroscopy is also useful to evaluate the degree of magnetization vector tilting from line intensity ratio [13]. For example in Fe/Co multilayers a magnetic morphology characterized by stripe domains appears in spite of a planar or uniaxial in-plane anisotropy is normally expected. These stripe domains are due

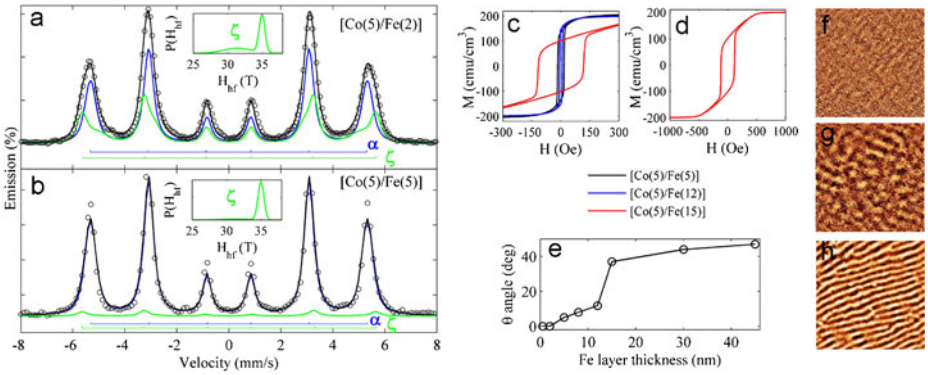

Fig. 4 CEMS spectra for **a** [Co(5)/Fe(2)] and **b** [Co(5)/Fe(5)], AGFM loops for **c** [Co(5)/Fe(t_{Fe})] t_{Fe} = 5,12,15 nm and **d** [Co5/Fe15], **e** angle between the magnetization vector and the film plane vs. the Fe layer thickness, MFM images for **f** [Co(5)/Fe(5)], **g** [Co(5)/Fe(12)] and **h** [Co(5)/Fe(15)]

to an out-of-plane magnetization component which determines an oscillation of the magnetic moments in and out of the film plane.

Co/Fe multilayers were grown at room temperature onto glass substrates by an UHV-MBE system, the Co thickness was fixed at 5 nm while the Fe layer thickness was changed in the range 0.5–15 nm [Co(5)/Fe(t_{Fe})], and finally capped by a Co layer 5 nm thick.

Figure 4a–b show the CEMS spectra for [Co(5)/Fe(2)] and [Co(5)/Fe(5)] multilayers fitted by superimposing to a main contribution due to α-Fe, a series of sextets (ζ) due to an interface region constituted by an FeCo equiatomic compound (main peak at 350 kOe) and an Fe-containing Co solid solution (lower H_{hf} tail). By increasing the Fe layer thickness this interfacial region decreases and the solid solution tends to disappear Fig. 4b**,** reasonably because of the formation of a more continuous and compact structure that (i) lowers the Fe/Co intermixing and (ii) favours the formation of the ordered FeCo equiatomic compound.

The hysteresis loops (Fig. 4c) show for the multilayers with Fe layer thickness lower than 5 nm the presence of a significant in-plane uniaxial anisotropy, absence of a magnetic morphology (Fig. 4f). For Fe layer thickness higher than 5 nm the hysteresis loops appreciably change with the appearance of a "transcriptical" shape indicating the establishing of an out-of-plane contribution to the magnetization vector able to give rise to a stripe-like domain pattern (Fig. 4g). The strength of this out-of-plane component (Fig. 4d) and the MFM signal appreciably increase by increasing the Fe layer thickness up to 15 nm at which long and parallel domains appear (Fig. 4h). From the line intensity ratio of the CEMS spectra, the tilting of the magnetization vector is evaluated and summarised in Fig. 4e as a function of the Fe layer thickness.

The knowledge of magnetization tilting allows one to evaluate the energy density contributions to the system in order to understand the origin of the perpendicular anisotropy. In the case of Fe/Co multilayers, the perpendicular moment tilting can be due to a negative magnetoelastic energy density [14] able to overcome the shape anisotropy. This, however, strengthens by decreasing the multilayer thickness, giving rise to reorientation of the easy orientation axis into the film plane.

References

1. Pérez-Alonso, F.J., Ojeda, M., Herranz, T., González-Carballo, J.M., Fierro, J.L.G., Bengoa, J.F., Marchetti, S.G.: Open Magn. Reson. J. **1**, 64–70 (2008)
2. Leendert Bezemer, G., Remans, T.J., van Bavel, A.P., Dugulan, A.I.: J. Am. Chem. Soc. **132**, 8540–8541 (2010)
3. Carbucicchio, M., Martini, C., Palombarini, G., Rateo, M.: Hyperfine Interact. **139/140**, 259–265 (2002)
4. Palombarini, G., Carbucicchio, M.: Hyperfine Interact. **111**, 101–111 (1998)
5. Nowik, I., Felner, I., Awana, V.P.S., Vajpayee, A., Kishan, H.: J. Phys. Condens. Matter **20**, 292201 (2008)
6. Sharma, K., Reddy, V.R., Kothari, D., Gupta, A., Banerjee, A., Sathe, V.G.: J. Phys. Condens. Matter **22**, 146005 (2010)
7. Carbucicchio, M., Ciprian, R., Micele, L., Palombarini, G.: J. Phys. Conf. Ser. **217**, 012080 (2010)
8. Ciprian, R., Palombarini, G., Carbucicchio, M., Sambogna, G.: Hyperfine Interact. **192**, 43–49 (2009)
9. Carbucicchio, M., Meazza, G., Palombarini, G.: J. Mater. Sci. **17**, 3123–3128 (1982)
10. Carbucicchio, M., Martini, C., Palombarini, G., Rateo, M.: Phil. Mag. B **76**, 669 (1997)
11. Ciprian, R., Carbucicchio, M., Turilli, G.: Hyperfine Interact. **191**, 33–40 (2009)
12. Carbucicchio, M., Ciprian, R.: Sol. State Comm. **152**, 189–193 (2012)
13. Carbucicchio, M., Rateo, M.: Hyperfine Interact. **141/142**, 441–446 (2002)
14. Ausanio, G., Iannotti, V., Lanotte, L., Carbucicchio, M., Rateo, M.: J. Magn. Magn. Mater. **226/230**, 1740–1742 (2001)